Geophysical Journal International

Geophys. J. Int. (2010) doi: 10.1111/j.1365-246X.2010.04811.x

GPS and gravity constraints on continental deformation in the Alborz mountain range, Iran

Yahya Djamour,[1,*] Philippe Vernant,[1] Roger Bayer,[1] Hamid Reza Nankali,[2] Jean-François Ritz,[1] Jacques Hinderer,[3] Yaghoub Hatam,[1,2] Bernard Luck,[3] Nicolas Le Moigne,[1] Morteza Sedighi[2] and Fateme Khorrami[2]

[1] *Lab. Geosiences Montpellier, University Montpellier* 2 – *CNRS,* 34095 *Montpellier, France. E-mail: pvernant@um2.fr*
[2] *National Cartographic Center (NCC), Meraj Av., Azadi square, P.O. Box* 13185–1684, *Tehran, Iran*
[3] *EOST/IPGS (UMR* 7516*)* 5 *rue Descartes,* 67084 *Strasbourg Cedex, France*

Accepted 2010 September 13. Received 2010 September 13; in original form 2010 April 28

SUMMARY

A network of 54 survey GPS sites, 28 continuous GPS stations and three absolute gravity (AG) observation sites have been set up in the Alborz mountain range to quantify the present-day kinematics of the range. Our results allow us to accurately estimate the motion of the South Caspian block (SCB) for the first time, and indicate rotation of the SCB relative to Eurasia, accounting for the left lateral motion in the Alborz range. In light of these new results, it clearly appears that deformation rates vary along the range, the eastern part accommodating mainly left lateral strike slip (2 mm yr^{-1} south of the range and 5 mm yr^{-1} north of the range) with a very low range normal shortening rate on the Khazar thrust fault ($\sim$2 mm yr^{-1}), and the western part accommodating range normal shortening ($\sim$6 mm yr^{-1}) on the Khazar thrust fault with a left lateral component of $\sim$2 mm yr^{-1} north of the range and 1 mm yr^{-1} south of the range. These present-day kinematics agree with geomorphologic estimated slip rates, but not the long-term deformation, corroborating the idea that the kinematics of the range have changed recently due to the change of SCB motion.

Modelling of the interseismic deformation suggests a deep locking depth on the central-western segment of the Khazar fault ($\sim$30 km) in agreement with the Baladeh earthquake rupture and aftershock ranging between 10 and 30 km. Given this unusual deep locking depth and the 34° dip of the thrust, a large part of the Alborz range is located above the seismically coupled part of the fault. Based on our AG measurements this part of the range seems to uplift at a rate of 1–5 mm yr^{-1}, in agreement with terrace uplift.

Key words: Satellite geodesy; Gravity anomalies and Earth structure; Plate motions; Intra-plate processes; Neotectonics.

1 INTRODUCTION

The Alborz mountain range encircles the South Caspian Basin from the Talesh to the Kopeh Dag mountains (Fig. 1). Numerous active faults strike mainly parallel to the belt and form a 'V' shaped pattern (Berberian 1983; Berberian & Yeats 2001; Allen *et al.* 2003b; Ritz *et al.* 2006), with WNW–ESE trending faults in Western Central Alborz passing abruptly to ENE–WSW trending faults in the Eastern Central Alborz (Fig. 1). Numerous strong historical earthquakes are reported in the Central Alborz (Tchalenko 1975; Ambraseys & Melville 1982; Berberian & Yeats 1999; Berberian & Yeats 2001) indicating rather high seismic activity, a result supported by the instrumental seismicity (Engdahl *et al.* 2006). The centroid moment tensors (CMT) of the Harvard Catalogue for earthquakes larger than M_w 5.0 (http://www.globalcmt.org) and complemented by the CMT solutions computed by Jackson *et al.* (2002) for events larger than M_w 5.4 (Fig. 1) show that the present-day deformation in Alborz is characterized by range-parallel left-lateral strike-slip and thrust faults. Located at the immediate southern foothills of the Central Alborz, historical sites in the Tehran region have been destroyed several times by earthquakes in the past (Ambraseys & Melville 1982; Berberian & Yeats 1999) and the present-day Tehran megapole (12 million people) is facing a critical seismic hazard. No large earthquake has occurred since 1830, but the recent M_w 6.2 Baladeh earthquake in 2004 (Tatar *et al.* 2007), though 70 km further north (Fig. 1), served as a reminder of the risk encountered if one of the closer faults break, which is likely to occur since most of the deformation is accommodated by seismic processes (Masson *et al.* 2005).

*Now at: Geomatics College, National Cartographic Center (NCC), Meraj Av., Azadi square, P.O. Box 13185-1684, Tehran, Iran.

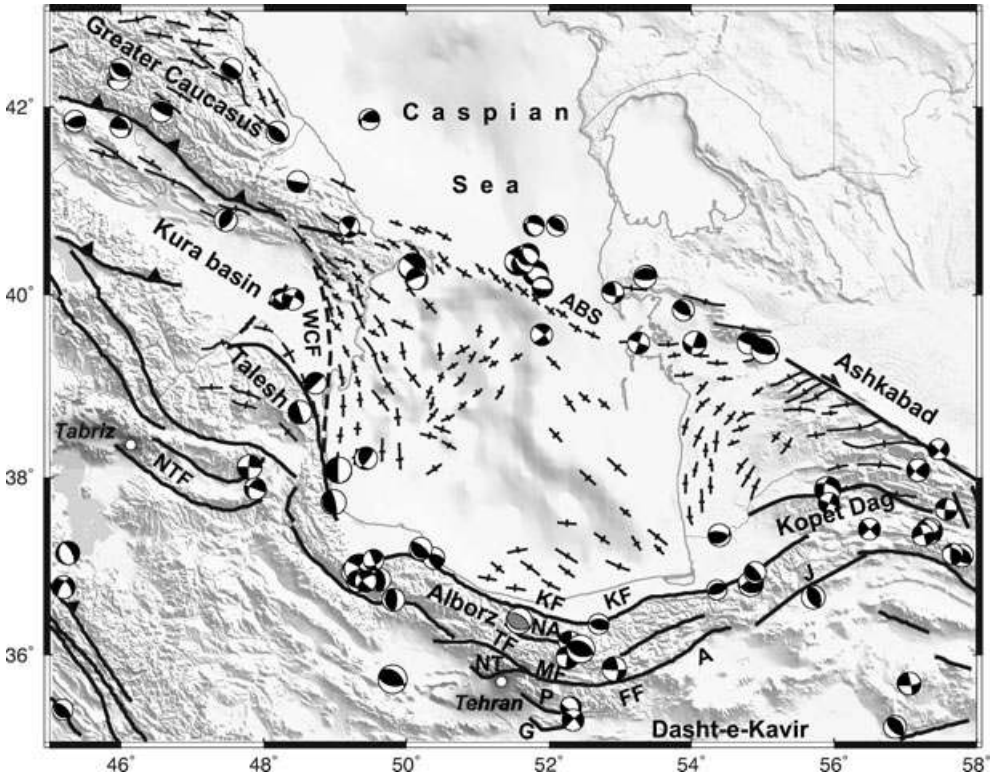

Figure 1. Summary structural map adapted from Jackson *et al.* (2002), the black focal mechanisms are from Jackson *et al.* (2002), the grey one (Baladeh earthquake) is from Tatar *et al.* (2007). A, Astaneh fault; ABS, Apsheron-Balkhan sill; FF, Firuzkuh fault; G, Garmsar fault; J, Jajarm fault, KF, Khazar fault; MF, Mosha fault; NA, North Alborz fault, NT, North Tehran fault; NTF, North Tabriz fault; P, Parchin fault; TF. Taleghan fault; WCF, West Caspian fault.

The main active thrust structures bound the range to the north (North Alborz and Khazar (hidden) south-dipping thrust faults, Fig. 1) and to the south (North Tehran, Garmsar and Parchin north-dipping thrust faults), while the left-lateral strike-slip deformation concentrates inside the mountain range, in its southern half, along the Taleghan, Mosha, Firuzkuh and As left-lateral strike slip faults. In terms of historical seismicity, three historical earthquakes with magnitudes greater than 6.5 occurred along the eastern part of the northern faults during the last two centuries, and active microseismicity is present in this area (Ashtari *et al.* 2005). On the southern side of the range, three historical earthquakes were reported in 958 AD ($M_s \sim 7.7$), 1665 AD ($M_s > 6.5$) and 1830 AD ($M_s \sim 7.1$) (Berberian & Yeats 1999). From morphotectonics and structural analyses, Allen *et al.* (2003a) and Bachmanov *et al.* (2004) deduced the left-lateral motion of the Mosha fault, to which the later authors identified an additional reverse component. Analyzing the morphology in detail with digital elevation models and palaeoseismology, Ritz *et al.* (2006) and Nazari *et al.* (2009) concluded that the left-lateral motion along the Taleghan–Mosha–Firuzkuh faults was associated with normal faulting, and that these transtensional kinematics are active since the Middle Pleistocene (<1.5 Myr), implying a recent change in the tectonic regime as suggested also by Landgraf *et al.* (2009) and Solaymani *et al.* (2010). The present-day microseismicity south of the range is mainly concentrated near the eastern branch of the Mosha fault and the focal mechanism solutions are consistent with the left-lateral normal motion observed along a steep north-dipping fault Ashtari *et al.* (2005). The North Tehran and the Parchin thrust faults dip northward and limit the relief of the Central Alborz to the south and could have been the sources of historical earthquakes in 312–280 BC ($M_s \sim 7.6$), 743 ($M_s \sim 7.2$), 855 ($M_s \sim 7.1$), 1177 ($M_s \sim 7.2$) and 1384 AD (Ambraseys & Melville 1982; Berberian & Yeats 1999).

The recent geodynamic evolution of the Central Alborz has been attributed to strain partitioning of oblique shortening (Jackson *et al.* 2002; Allen *et al.* 2003b). This would be the result of a transpressive regime that started during the Pliocene (3–5 Ma) and would be associated with the southwestward displacement of the South Caspian Basin with respect to the Central Iran Block. Before this epoch and since the Miocene, NS shortening occurred in Alborz and was distributed on fan shaped thrusts dipping inwards from the limits of the belt, associated with right-lateral and left-lateral strike-slip movements within the western and eastern parts of the range, respectively (Allen *et al.* 2004). This tectonic setting resulted in an uplift of the central part of the belt between 6 and 4 Ma (Axen *et al.* 2001). On the base of estimates of slip rates and total displacements along left-lateral strike-slip faults (i.e. Astaneh, Jajarm faults, Fig. 1), Hollingsworth *et al.* (2008) proposed that the strain partionning in Alborz associated with the southwestward motion of the South Caspian Basin was two times older (i.e. 10 Ma).

On the other hand, Ritz *et al.* (2006) proposed that the motion of the South Caspian Basin (southwestward motion and clockwise rotation) was much younger. Their interpretation is based on the fact that the general left-lateral wrenching of the belt (which is related to the South Caspian Basin motion) shows a normal component due to the obliquity of some of the faults (e.g. Taleghan, Mosha) with respect to the general trend of the range, and that the cumulated topography associated with this normal component is small and has not yet reversed the relief. Ritz *et al.* (2006) point out that the kinematical change (from mainly reverse to left-lateral-normal) occurs contemporaneously with the Damavand volcanic activity.

The first estimation of the present-day kinematic of the central Alborz results from a survey mode GPS (SGPS) profile across the central Alborz (Vernant *et al.* 2004a). However, the SGPS sites were sparse and only the bulk N–S shortening (5 ± 2 mm yr^{-1}) and a global left lateral motion (4 ± 2 mm yr^{-1}) could be estimated. Since then, several more SGPS sites have been implemented as well as a continuous GPS (CGPS) network. Moreover, precise absolute gravity (AG) measurements have been repeated across the range in order to better constrain the uplifting rate.

In this paper, we present our latest GPS velocity field and we interpret the present-day kinematics of the Alborz mountain range using an elastic block model. We use the gravity measurements to estimate the rate of uplift of the range. Then, we combine these results to investigate the active tectonics and geodynamics of the region.

2 GPS OBSERVATIONS AND PROCESSING

Our network consists of 54 SGPS sites implemented in the Alborz in the framework of a cooperative program between the French Centre National de la Recherche Scientifique (CNRS) and the Iranian National Cartographic Center (NCC) and 28 CGPS sites implemented by the NCC. This network spreads from the Caspian Sea to the north to the Central Iranian desert to the south (Fig. 2). Average distance between two sites is 10 km around Tehran and 30–70 km elsewhere. Most of the sites are anchored in bedrock. The others consist of geodetic pillars or concrete blocks installed in consolidated sediments.

The SGPS sites were surveyed at least three times from 2000 to 2008. All SGPS sites were measured with Ashtech Z12 and Trimble 4000SSI receivers equipped with choke-ring antennas. The CGPS sites were installed since 2005, and all but FOIM have at least three years of continuous recording.

We use the GAMIT/GLOBK software package (Herring *et al.* 2009a,b,c) to compute the coordinates and velocities of the sites, using a three-step strategy (Feigl *et al.* 1993; Dong *et al.* 1998). GPS data of 14 IGS stations were introduced in the process to tie our local network to the ITRF reference frame. Our local quasi-observations were combined with the global quasi-observations provided by MIT (http://www-gpsg.mit.edu/ŝimon/gtgk/index.htm) from 1996 to 2008 day of year 245. Following Reilinger *et al.* (2006), we account for the correlated errors in the time-series by calculating a unique noise model for each CGPS station. The algorithm used to model the data noise spectrum assumes that each time-series can be adequately modelled using a first-order Gauss Markov (FOGM) process noise (Gelb 1974). The FOGM is estimated from individual stations time-series by averaging the residuals over increasingly longer intervals that range from a minimum of 7 d to a maximum of 1/10th of the total time-series span. For each interval we compute the Chi-square per degree of freedom (d.o.f.). To the opposite of a white process noise, the Chi-square/d.o.f. values of non-white noise spectra increase with increasing averaging time. The

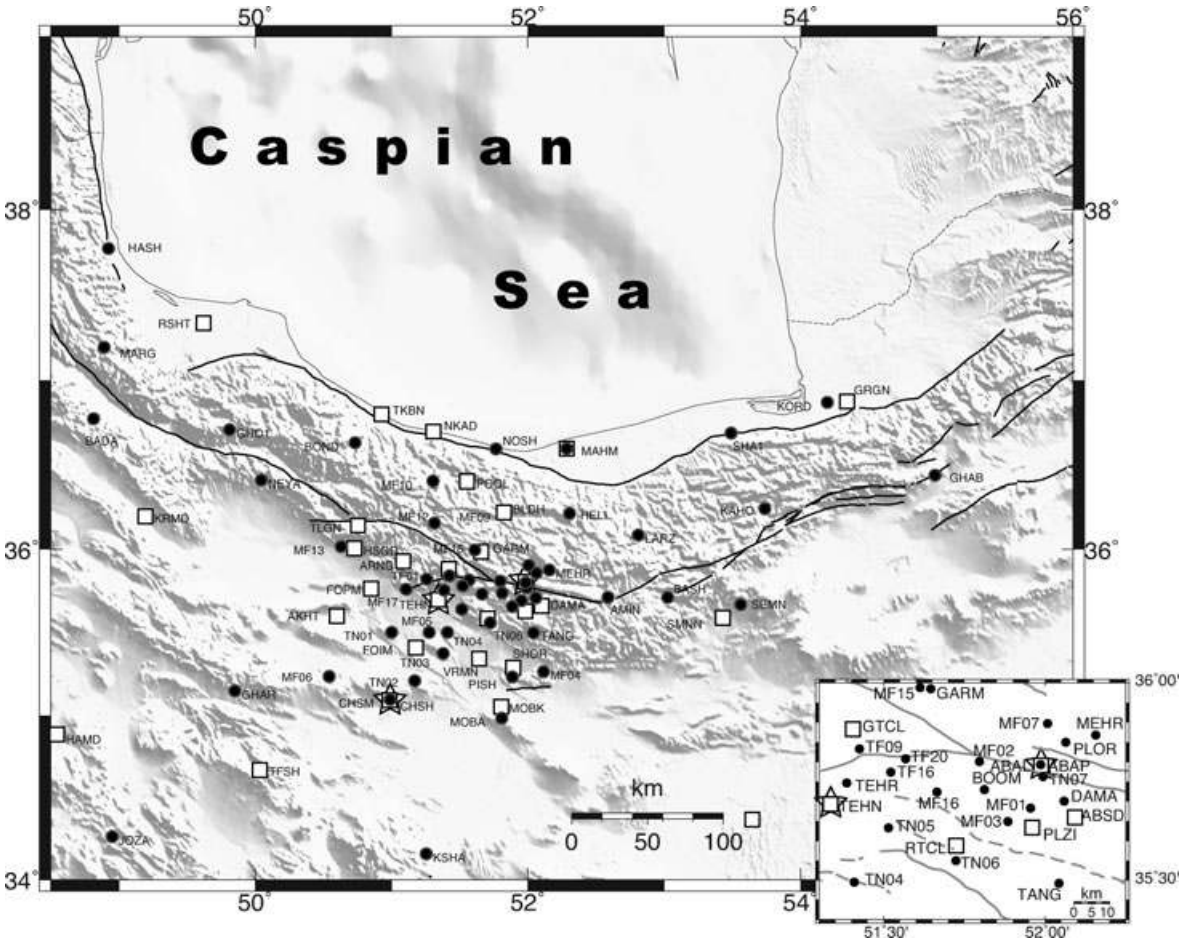

Figure 2. Location of the CGPS (squares), SGPS (circles) and gravity (stars) sites used in this study, the inset is for the eastern Tehran region.

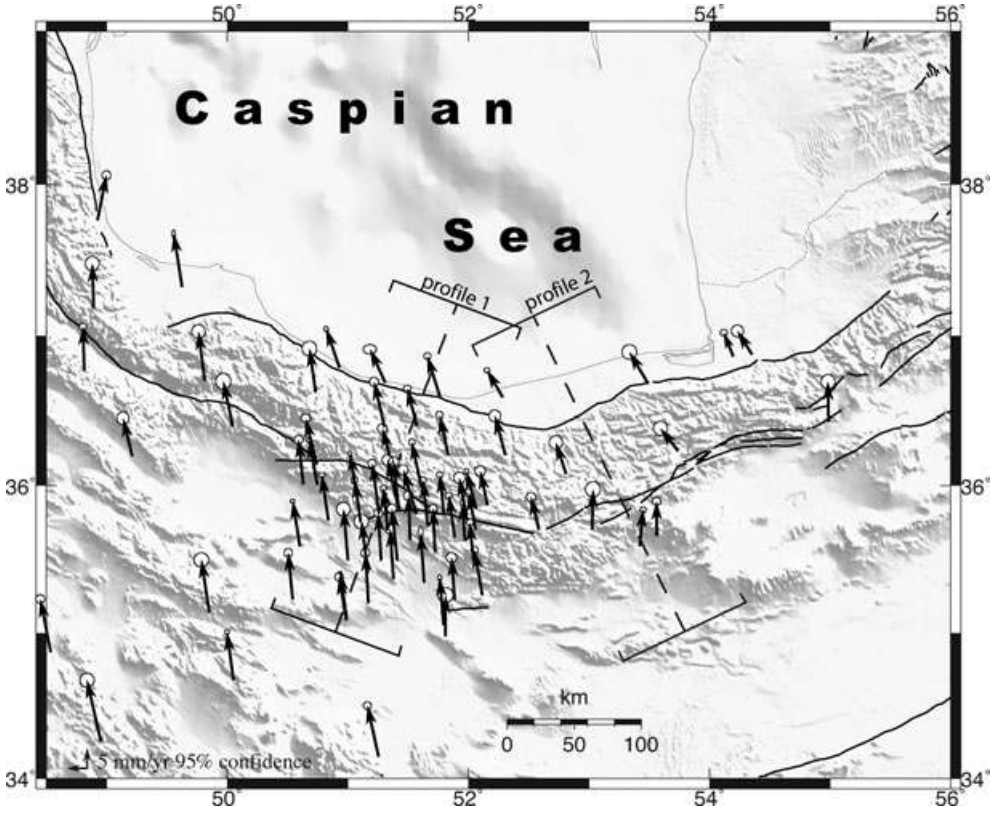

Figure 3. Map showing decimated GPS velocities and 95 per cent confidence ellipses relative to Eurasia determined in this study (all velocities are given in Table 1). The location and width of the two trans-Alborz velocity profiles plotted in Fig. 8 are also shown.

interval-averaged Chi-square/d.o.f. values are then fit to the FOGM model where a correlation time and long-term variance are estimated. This estimated FOGM model is then used to predict the site velocity uncertainty based on the time span of the time-series. The equivalent random-walk noise values obtained for the Alborz CGPS sites range from 0.25 to 1.2 mm $(\sqrt{\text{yr}})^{-1}$ in horizontal and 0.8–4.1 mm $(\sqrt{\text{yr}})^{-1}$ in vertical. The upper value of 1.2 mm $(\sqrt{\text{yr}})^{-1}$ in horizontal is for one station (VRMN), all the other being less or equal to 0.8 mm $(\sqrt{\text{yr}})^{-1}$, therefore we choose to use this value to estimate the SGPS horizontal uncertainties. For the vertical random walk noise value, 4.1 mm $(\sqrt{\text{yr}})^{-1}$ corresponds to the CGPS site PLOR, all the others are less or equal to 3 mm $(\sqrt{\text{yr}})^{-1}$, therefore we use 3 mm $(\sqrt{\text{yr}})^{-1}$. Finally, velocities and their 1σ confidence uncertainties were estimated in ITRF2005 and then the Eurasian reference frame was defined by minimizing the horizontal velocities of 23 IGS stations located in Europe and Central Asia (ARTU, BOR1, BRUS, GRAS, GRAZ, IRKT, JOZE, KOSG, KSTU, MADR, METS, NYAL, ONSA, POTS, TIXI, TOUL, TROM, VILL, WTZR, YAKT, ZECK, ZIMM and ZWEN). The WRMS value for the velocity residuals of these 23 sites is 0.48 mm yr^{-1}. There is good agreement between the SGPS and CGPS velocities for nearby Iranian sites since the differences are lower than 1 mm yr^{-1}. The GPS velocities and their uncertainties are shown on Fig. 3 and given in Table 1 in a Eurasia-fixed reference frame.

3 GPS VELOCITY FIELD AND BLOCK MODEL

The most striking, and systematic aspect of the velocity map shown in Fig. 3 is the azimuth change of the vectors from almost due north for the sites south of the Alborz range to NNW for the sites along the south Caspian shore. This indicates that, as noted earlier (Jackson *et al.* 2002; Allen *et al.* 2003a; Bachmanov *et al.* 2004; Vernant *et al.* 2004b; Ritz *et al.* 2006), left lateral strike slip is occurring in the Alborz range. Another striking aspect is the rather abrupt change in velocity along the south Caspian shoreline. Indeed, velocities north of the western Alborz (RSHT, TKBN, NKAD and NOSH) are ∼3 mm yr^{-1} faster than the eastern sites (MAHM, SHA1, KORD and GRGN) in the Eurasia fixed reference frame. Furthermore, the site SHA1 shows a velocity that is in between the average velocities of the eastern and western sites. This suggests that the GPS sites northeast of Alborz are farther away from the main active thrust fault than the northwestern GPS sites, consistent with the mapped location of the Kahzar thrust fault except for the site RSHT. Another explanation could be that western and eastern Alborz have different kinematics.

To investigate further this issue and to estimate fault slip rates for the main active faults, we use a block model. Several authors (e.g. McCaffrey 2002; Meade *et al.* 2002; Meade & Hager 2005) have demonstrated that, to first order, elastic block models can be used to fit the interseismic velocity field. No significant earthquake has occurred during the time interval of the measurements and the time-series of the closest SGPS sites (MF09, MF10, MF12 and NOSH) and CGPS sites (POOL and BLDH) from the Baladeh earthquake (M_w 6.2, 2004) do not show any significant coseismic nor post-seismic deformation. Furthermore, the last large earthquake of the region occurred in 1935. Hence our GPS measurements depict the interseismic deformation of the Alborz mountain range. We use McCaffrey's code (McCaffrey 2002) to solve for relative block motions by minimizing the GPS residual motions within the blocks in a least-square sense. The elastic strain accumulation on block

Table 1. East and north GPS velocity components (E Vel., N Vel.) and 1σ uncertainties (σE, σN) in a Eurasia-fixed reference frame as determined in this study are given in mm yr^{-1}. The correlation between E and N velocities (ρEN), residual velocities (Res E, Res N) from our preferred block model, are also given. An '$*$' in the site column designates continuous GPS stations. Block abbreviations are EU, Eurasia; AL, Alborz; CIB, central Iranian block; KA, Dasht-e-Kavir region; SCB, South Caspian Block.

Lon. (°E)	Lat. (°N)	E Vel.	N Vel.	σE	σN	ρEN	Site	Block	Res. E	Res. N
51.986	35.793	−1.17	9.96	0.52	0.51	0.014	ABAL	AL	0.84	0.63
51.987	35.793	−1.84	9.58	0.58	0.58	−0.002	ABAP*	AL	0.17	0.25
52.586	35.701	−2.01	8.2	0.47	0.46	0.01	AMIN	AL	−0.19	−0.87
51.829	36.208	−2.02	9.36	0.49	0.31	0.001	BLDH*	AL	0.63	−0.75
50.732	36.623	−1.52	10.85	0.74	0.76	0.004	BOND	AL	0.51	−0.2
51.646	35.985	−2.18	10.41	0.2	0.36	0.002	GARM*	AL	0.19	0.56
49.812	36.699	−1.53	12.29	0.68	0.71	−0.002	GHO1	AL	−0.13	−0.22
48.922	37.764	2.25	11.28	0.44	0.46	0.002	HASH	AL	2.17	−0.74
52.305	36.206	−2.57	9.68	0.58	0.56	0.023	HELI	AL	0.65	0.6
53.739	36.236	−4.38	5.56	0.71	0.72	0.003	KAHO	AL	−2.23	−2.1
52.811	36.078	−2.57	7.87	0.68	0.69	0.001	LARZ	AL	0.63	−0.42
48.891	37.187	−0.33	10.98	0.7	0.72	−0.011	MARG	AL	0.37	−2.63
52.157	35.868	−1.79	8.52	0.52	0.52	0.009	MEHR	AL	0.53	−0.8
51.797	35.801	−1.04	10	0.33	0.33	0.001	MF02	AL	0.89	0.42
52.008	35.897	−0.48	8.37	0.33	0.34	0	MF07	AL	1.85	−1.17
51.833	36.205	−2.15	9.87	0.36	0.36	0.004	MF09	AL	0.51	−0.23
51.304	36.394	−2.62	11.08	0.46	0.47	−0.002	MF10	AL	0.12	0.55
51.315	36.15	−1.23	11.63	0.54	0.54	0.006	MF12	AL	1.13	1.22
51.613	35.988	−2.46	11.26	0.33	0.33	−0.005	MF15	AL	−0.1	1.4
51.768	36.586	−3.22	10.37	0.37	0.34	0.005	NOSH	AL	0.06	1.33
52.064	35.85	−2.39	9.12	0.23	0.29	−0.002	PLOR	AL	−0.16	−0.24
51.574	36.403	−2.42	9.12	0.39	0.33	−0.001	POOL*	AL	0.5	−0.86
49.624	37.323	−2.07	13.26	0.17	0.41	−0.002	RSHT*	AL	−0.85	0.75
53.492	36.679	−4.71	7.93	0.74	0.76	0.006	SHA1	AL	−1	1.3
51.994	35.763	−1.83	9.34	0.47	0.48	0.012	TN07	AL	0.08	0.03
54.353	36.876	−3.63	5.83	0.61	0.61	0	GRGN*	SCB	−0.3	0.71
54.199	36.86	−2.41	6	0.36	0.34	0.006	KORD	SCB	0.97	0.73
52.285	36.588	−3.94	6.79	0.29	0.26	0.001	MAHM*	SCB	−0.3	−0.49
51.31	36.685	−3.82	8.38	0.66	0.49	0	NKAD*	SCB	−0.48	−0.21
57.308	37.814	−2.9	3.49	0.44	0.41	0.013	SHIR	SCB	−0.31	1.68
50.93	36.786	−3.3	9.68	0.24	0.26	−0.001	TKBN*	SCB	−0.19	0.62
48.005	37.169	−0.77	12.46	0.53	0.54	0.006	AGKA	CIB	0.97	0.31
53.822	32.313	−1.14	13.47	0.33	0.32	−0.001	ARDA	CIB	−0.58	−0.5
48.814	36.764	−0.34	11.07	0.35	0.35	0.001	BADA	CIB	1.48	−1.73
54.832	29.363	−0.77	13.73	0.41	0.39	0.003	BES2	CIB	−1.16	−0.6
47.93	36.232	−2.13	12.99	0.35	0.35	0.002	BIJA	CIB	−0.36	−0.21
48.183	36.607	0.34	11.52	0.66	0.69	−0.009	DAND	CIB	2.19	−1.48
56.504	28.529	4.64	13.95	1.04	0.95	−0.017	DENA	CIB	3.92	−0.04
49.851	35.14	−1.97	13.08	0.74	0.72	0	GHAR	CIB	−0.65	−0.4
57.217	28.01	2.07	14.69	0.98	0.89	−0.005	GHOL	CIB	1.66	0.61
48.534	34.869	−2.55	13.24	0.45	0.44	−0.002	HAMD*	CIB	−1.17	−0.2
54.608	30.079	0.69	13.3	0.41	0.38	−0.001	HARA	CIB	0.46	−1.12
48.952	34.256	−3.47	15.25	0.73	0.7	0	JOZA	CIB	−2.26	1.74
57.119	30.277	0.45	15.63	0.53	0.45	0	KERM	CIB	1.26	2.5
54.126	29.923	−1.29	14.25	0.41	0.39	0.006	KHO2	CIB	−1.48	−0.07
50.458	33.157	−2.81	12.9	0.75	0.72	0.005	KHON	CIB	−1.98	−0.88
47.123	37.368	−2.87	12.9	0.55	0.57	0.011	KHOR	CIB	−1.1	1.05
49.211	36.196	−2.3	9.44	0.61	0.61	0	KRMD*	CIB	−0.51	−3.61
51.255	34.15	−2.78	12.7	0.4	0.38	−0.002	KSHA	CIB	−1.43	−0.6
46.162	36.908	−2.31	13.47	0.37	0.35	0.001	MIAN	CIB	−0.38	0.4
51.799	32.25	−2.58	13.75	0.74	0.7	0.004	QOMS	CIB	−2.08	−0.28
45.887	38.228	1.43	11.93	0.37	0.37	0.006	SHAB	CIB	2.68	3.37
50.748	32.367	−2.34	12.51	0.4	0.37	−0.005	SHAH	CIB	−1.66	−1.25
49.668	33.073	−0.75	13.5	0.74	0.71	0.001	SHOL	CIB	0.18	−0.05
46.343	38.056	−0.74	13.51	0.52	0.53	0	TABZ*	CIB	0.1	4.19
50.052	34.676	−1.64	12	0.24	0.24	−0.003	TFSH*	CIB	−0.46	−1.6
52.091	35.661	−2	7.95	0.14	0.19	−0.003	ABSD*	KA	−0.59	−2.22
50.601	35.588	−1.77	11.31	0.24	0.18	−0.003	AKHT*	KA	−0.59	−0.72
51.075	35.928	−1.69	10.61	0.23	0.21	−0.002	ARNG*	KA	−0.45	−0.51
53.025	35.705	0.27	9.96	0.76	0.78	0	BASH	KA	1.38	0.57
51.812	35.73	−1.7	10.22	0.36	0.34	0	BOOM	KA	−0.25	−0.14

Table 1. (*Continued.*)

Lon. (°E)	Lat. (°N)	E Vel.	N Vel.	σE	σN	ρEN	Site	Block	Res. E	Res. N
50.988	35.088	−1.79	10.75	0.43	0.43	0.002	CHSH	KA	−0.29	−1.19
50.989	35.088	−1.53	11.74	0.18	0.16	−0.003	CHSM*	KA	−0.03	−0.2
52.059	35.701	−1.7	9.26	0.38	0.38	0.006	DAMA	KA	−0.18	−0.88
51.166	35.409	−1.6	12.82	0.73	0.74	0.001	FOIM*	KA	−0.38	1.27
50.84	35.765	−1.66	11.36	0.37	0.2	−0.001	FOPM*	KA	−0.55	−0.19
54.989	36.43	−0.17	9.79	0.71	0.72	0.009	GHAB	KA	0.42	2.26
51.41	35.882	−2.43	10.76	0.55	0.55	0	GTCL*	KA	−1.01	−0.02
50.747	36.007	−2.05	11.01	0.18	0.21	−0.002	HSGD*	KA	−0.85	−0.32
58.464	35.293	−0.08	5.31	0.34	0.33	−0.002	KASH	KA	0.23	−0.24
51.955	35.683	−1.38	9.59	0.42	0.42	−0.004	MF01	KA	0.04	−0.7
51.885	35.649	−1.48	10.5	0.32	0.32	−0.001	MF03	KA	−0.17	0.07
52.117	35.258	−1.98	11.27	0.36	0.36	0.003	MF04	KA	−0.79	0.56
51.277	35.493	−0.74	11.78	0.44	0.43	−0.002	MF05	KA	0.43	0.42
50.543	35.227	−1.12	11.7	0.43	0.43	0.002	MF06	KA	0.47	−0.69
50.632	36.009	−1.21	11.12	0.44	0.44	0.002	MF13	KA	−0.04	−0.38
51.665	35.724	−1.25	11.53	0.33	0.33	−0.001	MF16	KA	0.08	0.93
51.108	35.753	−1.51	10.47	0.32	0.33	−0.001	MF17	KA	−0.38	−0.8
51.808	34.977	0.07	10.31	0.77	0.76	0.04	MOBA	KA	1.52	−0.87
51.795	35.053	−0.99	11.86	0.22	0.26	−0.002	MOBK*	KA	0.4	0.71
50.045	36.401	−2.35	10.96	0.76	0.8	−0.003	NEYA	KA	−1.21	−1.1
51.885	35.224	−0.79	10.58	0.52	0.51	0.014	PISH	KA	0.46	−0.37
51.971	35.63	−0.63	9.25	0.25	0.31	−0.002	PLZI*	KA	0.67	−1.12
56.07	33.369	0.68	10.04	0.42	0.39	0.002	ROBA	KA	3.36	2.28
51.711	35.574	−1.28	10.51	0.3	0.19	−0.001	RTCL*	KA	−0.08	−0.26
53.564	35.662	−0.06	8.58	0.42	0.4	0.009	SEMN	KA	0.66	−0.81
51.884	35.277	−0.83	12.88	0.17	0.16	−0.003	SHOR*	KA	0.39	1.97
53.421	35.588	0.82	9.24	0.3	0.28	−0.001	SMNN*	KA	1.58	−0.28
52.043	35.492	−0.9	9.59	0.36	0.36	0.005	TANG	KA	0.26	−0.93
51.334	35.697	−1.15	10.52	0.31	0.3	0	TEHN*	KA	0.01	−0.57
51.386	35.747	−0.72	12.53	0.79	0.75	0.014	TEHR	KA	0.48	1.56
51.257	35.812	−1.68	12.48	0.42	0.42	0.01	TF01	KA	−0.48	1.43
51.425	35.833	−1.33	12.16	0.5	0.5	0.009	TF09	KA	0	1.35
51.522	35.774	−1.77	11.96	0.41	0.41	0.009	TF16	KA	−0.46	1.2
51.568	35.808	−3.27	11.04	0.51	0.52	0.013	TF20	KA	−1.86	0.4
50.745	36.144	−2.84	11.43	0.48	0.37	−0.001	TLGN*	KA	−1.43	0.23
51	35.493	−1.1	12.79	0.7	0.7	0.022	TN01	KA	0.08	1.13
51.17	35.203	−0.72	12.56	0.45	0.46	0.008	TN02	KA	0.64	0.88
51.379	35.366	−0.83	12.43	0.48	0.49	0.011	TN03	KA	0.4	1.08
51.409	35.495	−1.34	12.89	0.46	0.47	0.009	TN04	KA	−0.17	1.68
51.515	35.633	−0.38	11.01	0.49	0.5	0.01	TN05	KA	0.8	0.07
51.724	35.55	−0.52	10.91	0.4	0.4	0.008	TN06	KA	0.67	0.13
51.632	35.344	−0.82	12.32	0.25	0.63	−0.001	VRMN*	KA	0.4	1.21
58.56	56.43	−0.27	−0.04	0.11	0.12	−0.005	ARTU*	EU	−0.04	0.11
17.073	52.277	−0.07	0.18	0.13	0.1	−0.004	BOR1*	EU	0.18	0.13
4.359	50.798	−0.55	−0.45	0.1	0.08	−0.003	BRUS*	EU	−0.45	0.1
6.921	43.755	0.11	0.41	0.1	0.11	−0.004	GRAS*	EU	0.41	0.1
15.493	47.067	0.8	0.66	0.14	0.1	−0.004	GRAZ*	EU	0.66	0.14
104.316	52.219	−0.37	−0.85	0.22	0.12	−0.001	IRKT*	EU	−0.85	0.22
21.032	52.097	−0.03	0.32	0.09	0.08	−0.009	JOZE*	EU	0.32	0.09
5.81	52.178	−0.15	0.73	0.11	0.09	−0.002	KOSG*	EU	0.73	0.11
92.794	55.993	−1.05	−1.54	0.23	0.22	0.002	KSTU*	EU	−1.54	0.23
355.75	40.429	1.38	−1.42	0.1	0.1	−0.004	MADR*	EU	−1.42	0.1
24.395	60.217	0.28	−0.81	0.08	0.1	−0.005	METS*	EU	−0.81	0.08
11.865	78.93	−0.06	−1.02	0.08	0.1	0	NYAL*	EU	−1.02	0.08
11.926	57.395	−0.74	−0.44	0.08	0.11	−0.003	ONSA*	EU	−0.44	0.08
13.066	52.379	−0.35	0.18	0.23	0.23	−0.002	POTS*	EU	0.18	0.23
128.866	71.634	−0.13	0.06	0.14	0.15	0.005	TIXI*	EU	0.06	0.14
1.481	43.561	−0.88	1.03	0.45	0.44	−0.001	TOUL*	EU	1.03	0.45
18.938	69.663	−0.58	0.92	0.08	0.08	−0.005	TROM*	EU	0.92	0.08
356.048	40.444	−0.28	0.42	0.13	0.08	−0.001	VILL*	EU	0.42	0.13
12.879	49.144	−0.04	0.32	0.08	0.08	−0.005	WTZR*	EU	0.32	0.08
129.68	62.031	−0.98	−0.52	0.38	0.25	0.002	YAKT*	EU	−0.52	0.38
41.565	43.788	−0.54	0.66	0.11	0.08	−0.007	ZECK*	EU	0.66	0.11
7.465	46.877	0.49	0.61	0.11	0.09	−0.004	ZIMM*	EU	0.61	0.11
36.759	55.699	0.29	−0.2	0.12	0.14	−0.004	ZWEN*	EU	−0.2	0.12

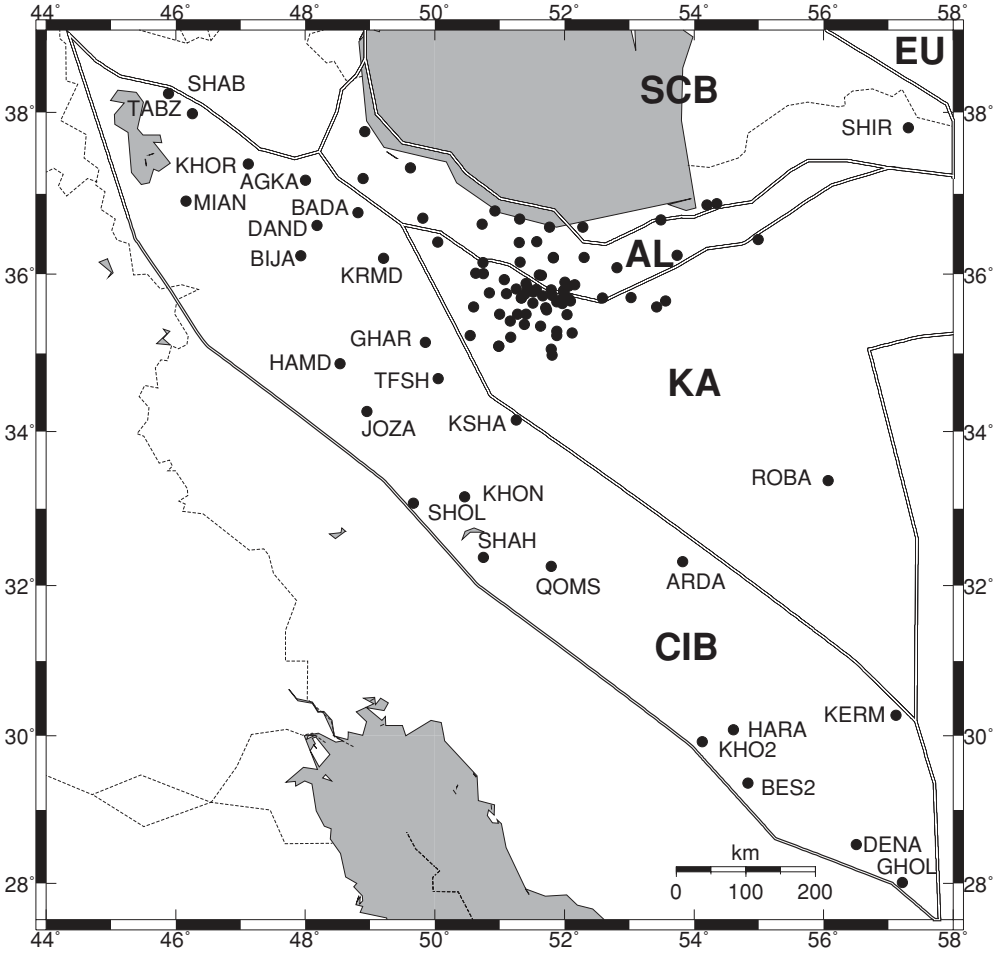

Figure 4. Map showing our preferred block model consisting of five plates/blocks. Abbreviations are Eurasian (EU), Alborz (AL), Central Iranian block (CIB), Dasht-e-Kavir (KA) and South Caspian (SCB).

bounding faults follows Okada's formulation (Okada 1985, 1992). The model allows no permanent deformation of the blocks or slip on unconnected faults, this implies that all the faults used must be on a block boundary.

25 GPS sites are located on the Alborz block (Fig. 4). North of Alborz, the motion of the South Caspian block (SCB) is constrained by six sites (GRGN, KORD, MAHM, NKAD, SHIR and TKBN). To the south, according to earlier studies (Vernant *et al.* 2004a, c), we use two blocks: the Central Iranian Block (CIB) and the Dasht-e-Kavir block. As the CIB and the Dasht-e-Kavir block encompass a region larger than our study we have also combined some of the data of (Walpersdorf *et al.* 2006; Masson *et al.* 2007) to have 25 sites on the CIB, 46 sites on the Dasht-e-Kavir and the site SHIR on the SCB (Fig. 4).

The block geometry is defined using the main active faults mapped in the region. The southern Alborz boundary corresponds to the main strike slip faults dipping steeply to the North (Taleghan, Mosha and Firuzku). According to Ashtari *et al.* (2005), the depth of microseismicity in the southern Alborz ranges from 0 to 16 km. Therefore, the modelled faults bounding the southern part of the Alborz block are assigned an 85° dip to the North and are locked from 0 to 16 km. The northwestern boundary of the Alborz block (heavy black line in Fig. 5) is rather poorly constrained by the geology and the geodesy, and no slip rates are estimated since we don't invert for the block motion west of these segments. The eastern boundary (longitudes greater than 55.5°E) is also poorly constrained by our GPS measurements, and several geometries could be used. The northern boundary of the Alborz block corresponds to the Khazar fault where the Baladeh earthquake involved slip at 10–30 km depth, with an average 34° south-dipping aftershock zone also restricted to the range 10–30 km (Tatar *et al.* 2007). In order to check if the GPS velocity field is consistent with a deeper than usual locking depth in this region and if aseismic slip could occur at shallow depth, we run several models where we vary the locking depth of the Khazar fault (black line, Fig. 6). The results suggest an optimum solution for a locking depth of 33 km. Although completely independent from the seismic study of Tatar *et al.* (2007), our results agree well with their findings. This deep locking depth is only possible for the central and western segments of the Khazar thrust fault since the residuals of the sites KAHO and GHAB are smaller with a shallower locking depth (10 km). We run a second set of experiments where we keep the depth of the locked Khazar fault equal to 33 km and we allow for an unlocked upper part of the fault (dashed line, Fig. 6). The results of this second set of experiments suggest that the upper part of the Khazar faults has to be locked to account for the geodetic observations.

Fig. 5 shows the residuals for each block (i.e. observed-modelled velocities) of our preferred model. The WRMS values for the Alborz, Caspian, CIB and Dasht-e-Kavir blocks are 0.85, 0.66, 1.45 and 0.80 mm yr^{-1}, respectively, with no significant systematic

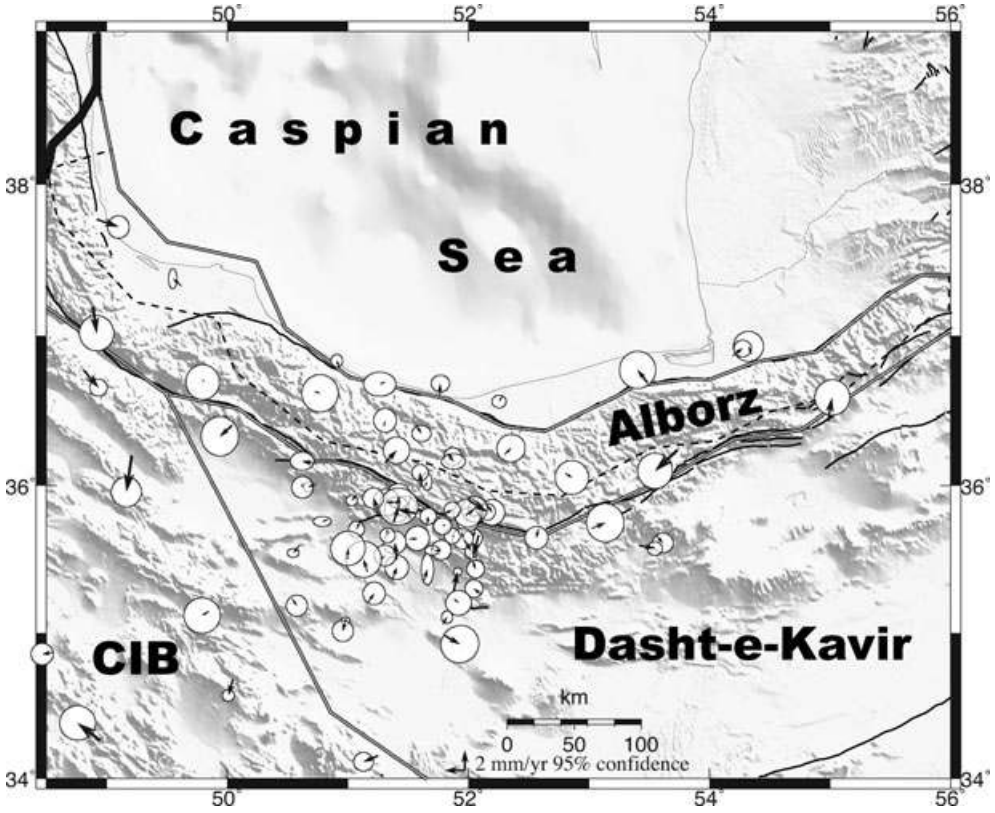

Figure 5. Map showing block model residual velocities (observed minus modelled) and 95 per cent confidence ellipses for the block model shown in Fig. 4 and described in the text. Light block boundaries show fault with estimated slip rate. Heavy black line in NW corner of the map shows block boundaries with no estimation of slip rate. The dashed line shows the estimated southern extent of the locked interface of the northern Alborz block boundary (Khazar fault).

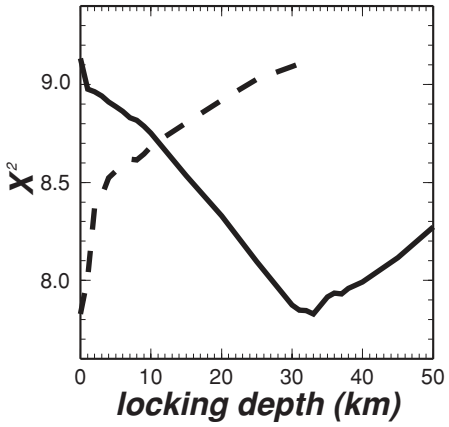

Figure 6. χ^2 plotted versus locking depth for the Khazar thrust fault. Black curve indicate the value for a locked fault from the surface down to the locking depth. Dashed curve indicates the value for a locked fault from the locking depth value down to 33 km depth.

residuals (Fig. 7). This fairly good fit to the data suggests that deformation in the Alborz range is well explained by a simple model with faults bounding the range to the north and south, the northern fault having a deeper locking depth (∼33 km) in its western part. Slightly higher residuals are seen on the western extremity of the Alborz Mountains, but given the sparse GPS coverage and the lack of geological studies of the active faults of this region, the models are very poorly constrained. The interseismic modelled deformation along the two profiles shows that, due to the orientation of the faults, the dominant faulting is mainly left lateral strike slip to the east and left lateral and thrust faulting to the west (Fig. 8).

Although the SCB is only constrained by six GPS sites, the slip rates obtained for the faults bounding the SCB to the South (Fig. 9) and to the north along the Apsheron Balkan sill (∼6 mm yr^{-1} of fault normal compression and ∼2 mm yr^{-1} of right lateral strike slip) and the Ashkhabad fault (∼1 mm yr^{-1} of fault normal compression and ∼3 mm yr^{-1} of right lateral strike slip) are reasonable. Therefore, at the longitude of the Alborz range the deformation related to the Arabia–Eurasia collision is accommodated almost equally on three main structures: Zagros, Alborz and the Apsheron-Balkan sill. The fault slip rates obtained for the main Alborz fault zones are given in Fig. 9. These slip rates correspond to a case where no off-fault deformation occurs and only one fault accommodates the differential motion between two blocks. Therefore the uncertainties on the slip rates depend only on the uncertainties on the Euler vectors and are ∼1 mm yr^{-1} along the southern Alborz region. The motion of the SCB is mainly based on GPS sites that are located very close to the southern boundary of the block, and therefore in the interseismic deformation zone along the faults. This implies that the slip rates estimated along the southern boundary of the SCB are maximum slip rates and their uncertainties are ∼2 mm yr^{-1}.

4 GRAVITY OBSERVATIONS AND PROCESSING

Since 2000, the AG field was surveyed in and nearby the Alborz range on three sites (Fig. 2): one is located within the range near the Mosha fault at an elevation of 3200 m (ABAL); another is located

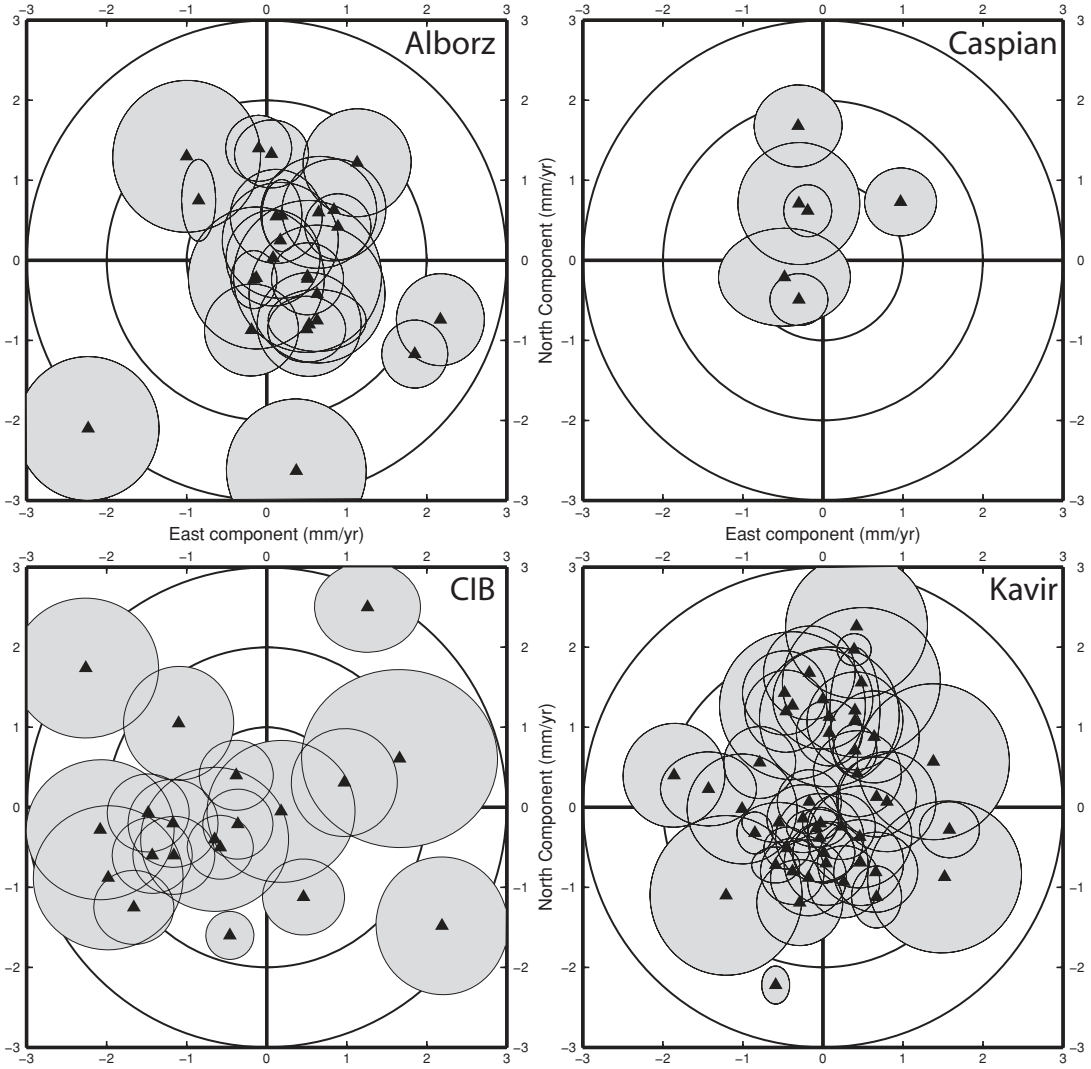

Figure 7. East and north component of the residuals of each block indicating no systematic misfit to the block model.

at the foothills of the range in Tehran city with an elevation of 1200 m (TEHN), and the last one is located in the desert zone 80 km south of Tehran where low seismic activity is reported (CHSH).

These sites where surveyed every year from 2000 to 2006. Each AG measurement took place in September–October, in order to minimize the variation of the seasonal component on the long-term fluctuations. The FG5#206 and FG5#228 absolute gravimeters belonging to the French national pool of gravimeters were used together with a Scintrex CG-3M microgravimeter to accurately estimate the AG value at each site.

The AG value g is estimated from the position of a dropping test mass as a function of time. The experimental protocol consists of estimating the mean value of g from 100 drops per hour. The 'drop to drop' precision on measurements at ABAL site was $\sim$5 μGal. Finally, the AG value was estimated by averaging the measurements over time periods greater than 12 hours. All the data sets were processed identically using the new processing software g-version 6.0 from Micro-g Solutions Inc. The geographical coordinates, the vertical gradient, and the nominal reference air pressure are fixed for each site. Models are applied to correct for the solid Earth tides (Wenzel 1994) and tidal ocean loading (FES2004, Lyard *et al.* 2006). Air pressure effects are corrected using the same barometric admittance and observed pressure data; finally, polar motion effects are subtracted using IERS observed pole coordinates.

With only one measurement per year, no coloured noise can be estimated from an analysis of our data set. The unknown coloured noise model for our data set should reflect hydrological and atmospheric effects in the Alborz. Indeed, the GRACE satellite experiments revealed seasonal (Wahr *et al.* 2004) and interannual variations (Andersen & Hinderer 2005) that can be fit with a global hydrological model (soil moisture). Using the European Centre for Medium-Range Weather Forecasts (ECMWF) and LadWorld global hydrological models to compute temporal variation of the terrestrial water storage and the associated gravity changes shows seasonal variations of 6–8 μGal in the Tehran area during the 2000–2007 epoch. These global models suggest that repeating the AG campaigns at the same epoch introduces a weak variation of the coloured noise ($<\mu$Gal). Hence, the 'hydrological and atmospheric colored noise' is neglected and we only rely on a white noise model being the sum of the instrumental high frequency noise and the setup noise ($\sim$1.6 μGal). However, gravity effects deduced from long wavelength terrestrial soil moisture LadWorld and ECMWF models ($>$100 km) do not account for local ground water induced gravity effects and their temporal variation due to water circulation. But this

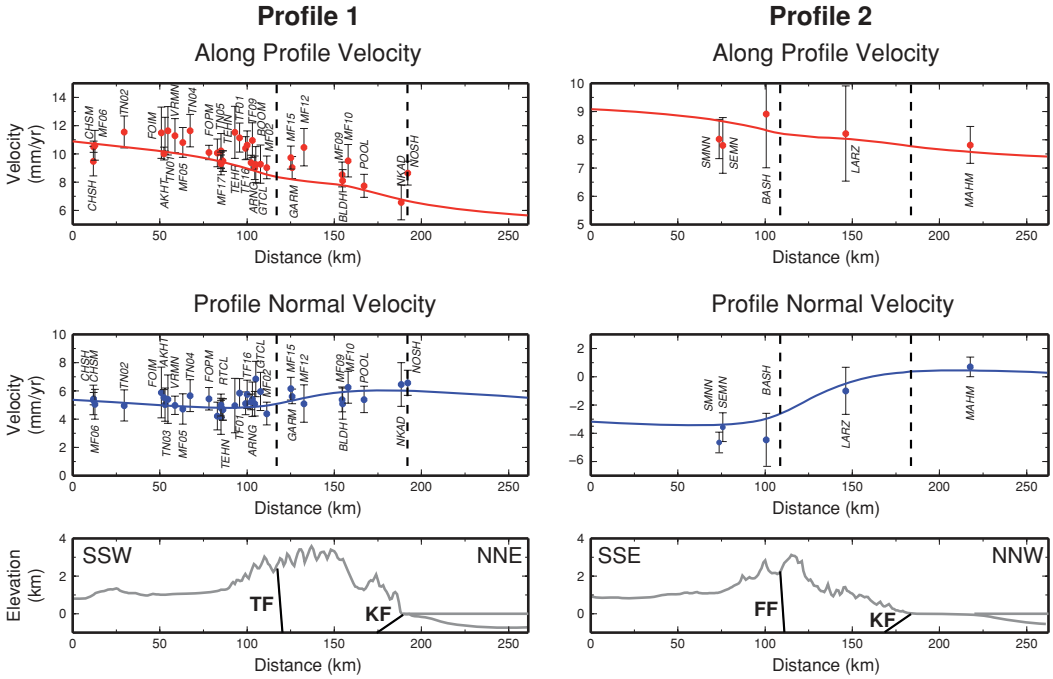

Figure 8. West (profile 1) and east (profile 2) Alborz velocity profile showing along profile, and profile normal velocities and 2σ uncertainties relative to Eurasia (see Fig. 3 for profile location and width). The curve is the theoretical strain accumulation obtained with the block model described in the text. The topography along the profile is extracted from the SRTM30 Plus database. TF, Taleghan fault; KF, Khazar fault; FF, Firuzkuh fault.

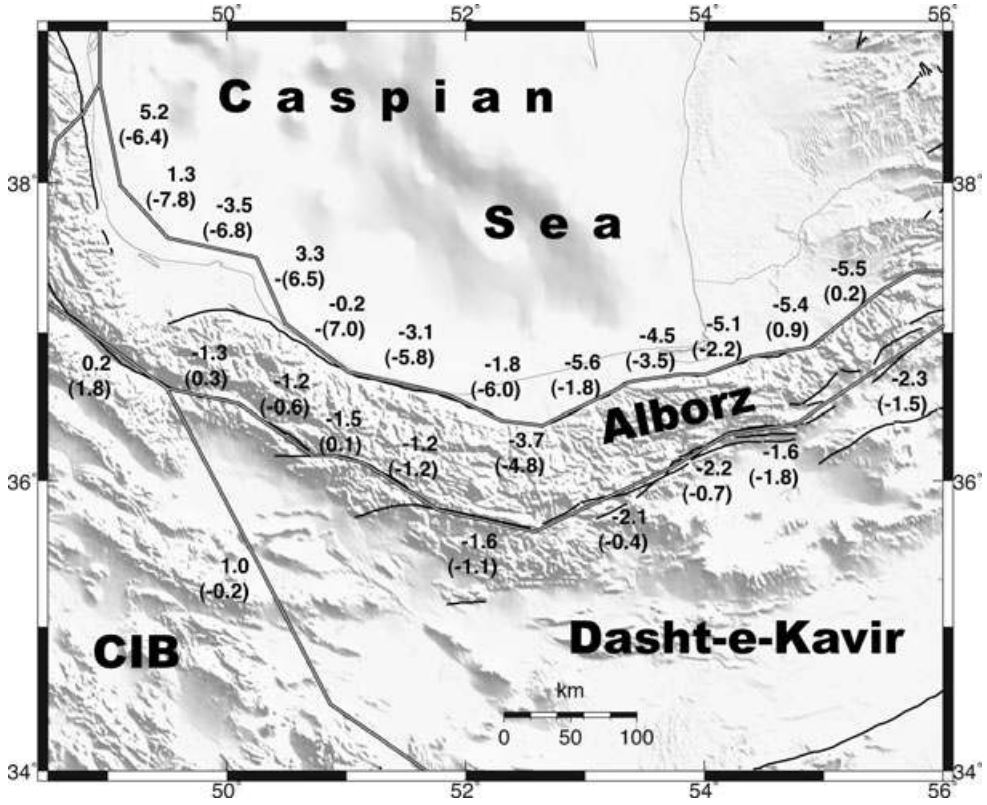

Figure 9. Map showing fault slip rates (mm yr^{-1}) deduced from the block model shown in Figs 4 and 5. Top numbers (no parentheses) are strike-slip rates, positive being right-lateral. Numbers in parentheses are fault-normal slip rates, negative being closing.

is the case for AG measurements at TEHN, since the temporal variations are mainly correlated with the depth of underground water tables beneath Tehran city. Therefore we do not report the AG values at TEHN. The temporal variations at Chesmeh-shour are lower than 2 μGal during the 2001–2006 interval but we do not have enough measurements to estimate a rate.

The site ABAL is located at 3200 m on the summit of a steep mountain attenuating the local hydrological related gravity changes.

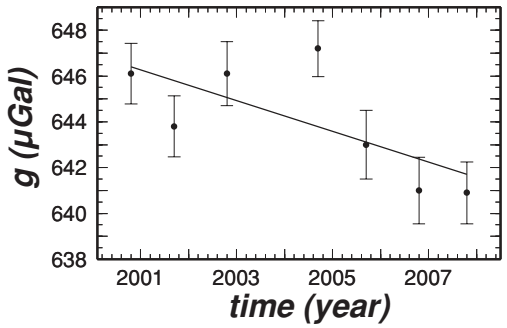

Figure 10. Time-series of the absolute gravity measurements at the site ABAL.

Estimating a rate of AG change for the ABAL station with either a white noise model or a statistical coloured noise model proposed by Van Camp *et al.* (2005) does not show significant differences, therefore we use the white noise model since we don't have enough data to constrain a coloured noise model. The rate inferred from AG time-series for the site ABAL is -0.67 ± 0.25 μGal yr^{-1} (1σ level) suggesting a low uplift rate (Fig. 10). Using the free-air gravity gradient, the gravity change $\delta g_z/\delta t$ due to the vertical displacement and erosion is given by

$$\delta g_z/\delta t(\mu\text{Gal yr}^{-1}) \approx -2\text{g}/a v_z \approx -0.3 v_z(\text{mm yr}^{-1}) \quad (1)$$

with g the gravitational acceleration, v_z the vertical rate and a the Earth's radius. Unfortunately, the AG values give the gravity variation δg that corresponds to the sum of the variation due to the mass distribution change (δg_m) and the vertical displacement (δg_z). Converting a rate of gravity change into a vertical velocity needs to account for lithospheric loading and mechanical response of the earth. In the case of postglacial rebound (PGR) and present-day ice sheet evolution, vertical uplift and gravity changes have been predicted for a large variety of mantle viscosities and elastic lithospheric thicknesses (Wahr *et al.* 1995; James & Ivins 1998). A factor of -0.16 μGal mm^{-1} was found, in agreement with AG observations in the northern part of the North American Plate (Larson & van Dam 2000).

In the mountain building processes, the lithosphere is flexed in response to tectonic loads (relief, subsurface loads). Goetze & Evans (1979) have shown that loads are supported for long periods of geological time ($>10^5$ yr) by a quasi-elastic layer that gives strength to the lithosphere. This elastic 'core' may be characterized by its flexural rigidity, or elastic thickness (Watts *et al.* 1980). The mechanical response of the lithosphere to topographic loads may be described in terms of an admittance function T, that is, free air anomaly/altitude ratio in the Fourier domain. Loads and isostatic deflection of the Moho are responsible for the free air gravity anomaly. In this study, the gravity change is associated with variation of the topographic load and correspond to the sum of the free air anomaly change and gravity perturbation due to vertical displacements. Using the relation (1), the rate of gravity change and the vertical rate are tied by the relation

$$T(k) = \delta G(k)/\delta Z(k) - 2g/a \quad (2)$$

with k the wavenumber in the Fourier domain, $\delta G(k)$ and $\delta Z(k)$ the Fourier transforms of the free air anomaly change $\delta g_z/\delta t$ and the vertical rate v_z. $T(k)$ may be predicted for an infinite thin elastic plate overlying an inviscid fluid (Karner & Watts 1983). Fig. 11 shows the admittance as a function of wavenumber (or wavelength λ of the relief change), for various elastic thicknesses ranging from 0 (local isostatic compensation) to 50 km (high rigidity). In the uncompensated waveband, $\lambda < 50$ km, the ratio is -0.19 μGal mm^{-1}. In the compensated waveband for $\lambda > 50$ km, the ratio depends on the elastic thickness of the lithosphere and varies from

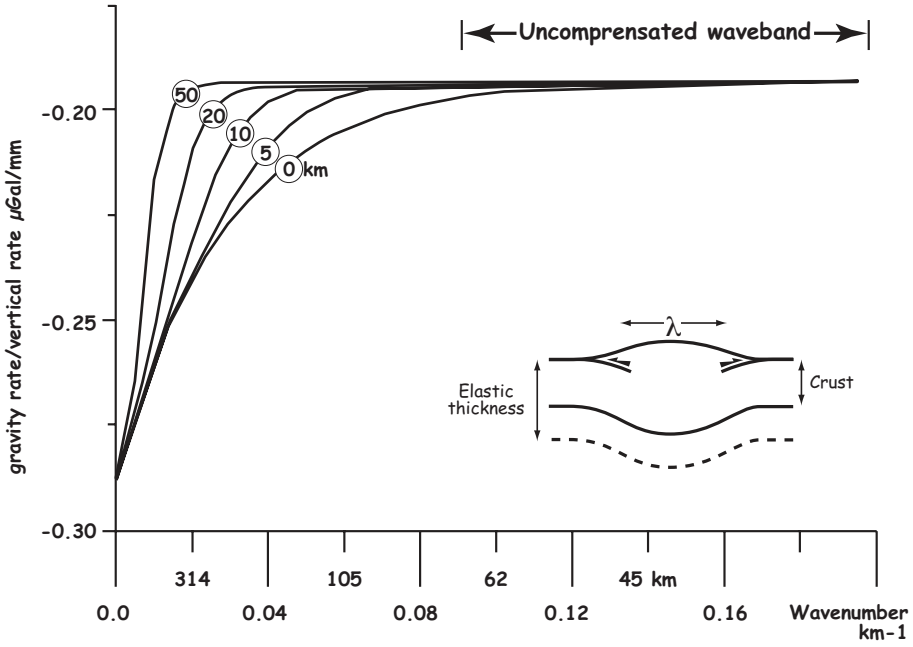

Figure 11. Admittance function versus wavenumber (gravity change/vertical change in Fourier domain). The continental lithosphere is considered as a homogeneous elastic plate overlying an inviscid fluid. The topography loads the lithosphere whose flexure depends on the wavelength of the relief and the elastic thickness of the plate. The temporal variation of the gravity field is the sum of the free-air anomaly change (relief and Moho effects) and the free-air variation due to vertical displacement. The admittance function is calculated for various elastic thicknesses from 0 to 50 km (crustal thickness: 30 km; crustal density: 2800 kg m^{-3}; density of the upper mantle 3300 kg m^{-3}). Note that the value of the admittance function within the 'uncompensated waveband' ($\lambda \leq$ 100 km) is ~ -0.2 μGal mm^{-1}.

Table 2. Euler vectors relative to Eurasia and 1σ uncertainties for the block model determined in this and prior studies. The number of GPS sites and WRMS residuals for each block in our model are also given. Plate abbreviations are EU, Eurasia; AL, Alborz; CIB, Central Iranian block; KA, Dasht-e-Kavir region; SCB, South Caspian Block. References are ts, this study; jm, Jackson & McKenzie (1984); re, Reilinger *et al.* (2006); ve, Vernant *et al.* (2004c).

Plates	Longitude (°E)	σ	Latitude (°N)	σ	Rate (deg Myr^{-1})	σ	WRMS	Number of sites	References
AL-EU	59.4	0.7	36.6	0.2	−0.969	0.072	0.85	25	ts
AL-EU	57.9	3.0	36.6	0.6	−1.299	0.790	1.95	4	re
SCB-EU	59.1	0.8	40.4	0.3	−0.622	0.055	0.66	6	ts
CIB-EU	−13.6	4.2	13.4	2.6	0.149	0.007	1.45	25	ts
CIB-EU	4.2	0.1	18.9	4.9	0.207	0.020	1.93	19	re
CIB-EU	0.98	1.2	23.15	13.2	0.189	0.1		6	ve
CIB-EU	65.8		27.5		0.56				jm
KA-EU	64.3	0.1	35.3	0.6	−0.61	0.024	0.80	47	ts
KA-EU	81.5	14.9	29.4	4.9	−0.225	0.124	1.42	8	re

−0.19 to −0.3 μGal mm^{-1}. This last value is close to the estimation of James and Ivins (1998) for an elastic spherical Earth (PREM model).

Therefore the absolute uplift rate at the site ABAL ranges between 3.5 and 2.2 ± 1.5 mm yr^{-1} with the admittance values of −0.19 and −0.3 μGal mm^{-1}, respectively. Vertical strain induced by tectonic loading for a site close to an active fault in a narrow mountain range such as Alborz is related to the interseismic deformation. The main strain accumulations near active faults occur over a width of usually less than 60 km on both sides of the active faults (Savage & Burford 1973). Therefore, from a spectral point of view, tectonic loading acts on the lithosphere in the uncompensated waveband domain and the admittance value may be close to the −0.2 μGal mm^{-1} value used by Meurers *et al.* (2007) in northwest Europe (Ardennes and Roer Graben). Hence the absolute uplift rate is more likely to be in the upper range of these estimates (∼3 mm yr^{-1}).

5 DISCUSSION

This study allows us to greatly improve the uncertainties of the estimation of Euler vectors obtained for the Alborz, Kavir and CIBs with respect to previous geodetic results (Vernant *et al.* 2004b; Reilinger *et al.* 2006). Moreover, we are able for the first time to estimate the SCB Euler vector from direct measurements (Table 2). The location of the SCB-Eurasia Euler vector explain why most of the deformation along the Ashkhabad fault is accommodated by right lateral strike slip (∼3 mm yr^{-1}) that evolves into a thrust fault north of the SCB (∼6 mm yr^{-1} of fault normal shortening). Given the position of the SCB-Eurasia pole of rotation close to the SCB, the motion of this block is more complicated than the 300° Azimuth vector suggested by Jackson *et al.* (2002) and Allen *et al.* (2003b) for the entire block. Indeed the velocity vector in a Eurasia reference frame for the SCB will change from 315°, south of the SCB to 000°, north of the SCB (Fig. 12).

Being able to estimate the motion of the SCB for the first time allows us to better determine the strike-slip and dip-slip on the faults bounding the Alborz range to the north (Fig. 9). South of the range along the Taleghan, Mosha, Firuzkuh and Astaneh faults, the fault normal component is not significant, indicating the mainly left lateral, strike slip character of these faults with a slip rate decreasing from ∼2 mm yr^{-1} in the eastern Alborz to ∼1 mm yr^{-1} in the western part of the range, which is consistent with morphotectonic studies (Ritz *et al.* 2006; Nazari *et al.* 2009). The lack of significant shortening (or extension) along these faults show that most of the shortening in Alborz occurs north of the range. However, several

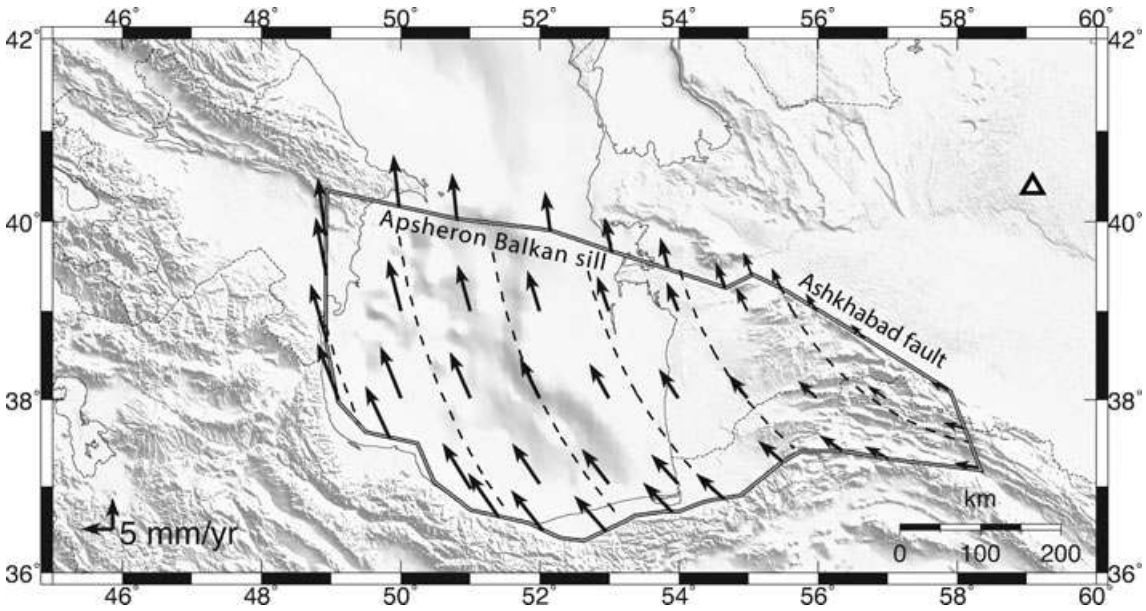

Figure 12. Location of the South Caspian/Eurasia Euler pole (triangle), predicted block motion direction (dashed lines and vectors) without taking into account the interseismic elastic strain along the block boundaries.

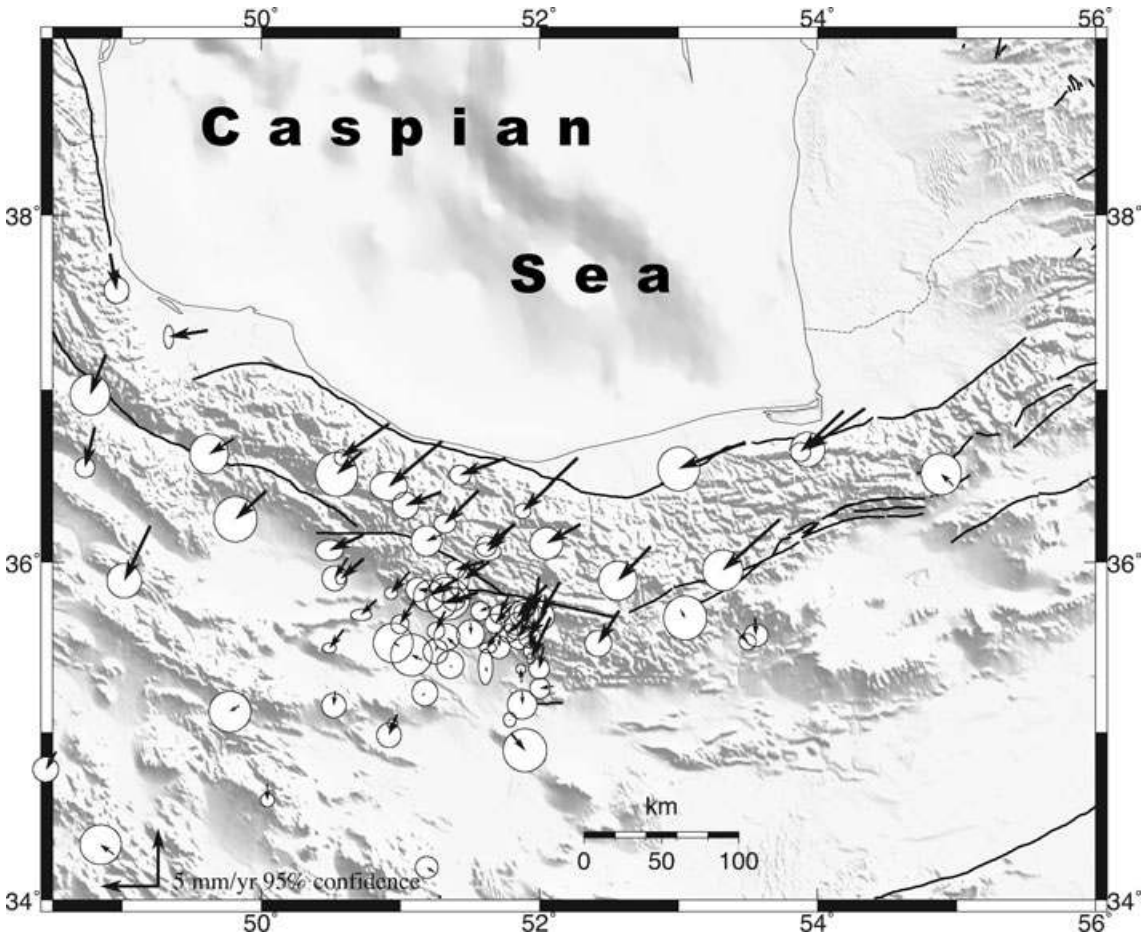

Figure 13. Map showing GPS velocities and 95 per cent confidence ellipses relative to the Dasht-e-Kavir region determined in this study.

thrust faults are reported along the southern foothills of the range such as the North Tehran thrust fault or the Parchin thrust fault (e.g. Berberian 1981; Landgraf *et al.* 2009), but the residuals within the Kavir block are lower than 1 mm yr^{-1} and for most of them not significant. This is consistent with results estimated from palaeoseismological studies and show that the slip rates of these reported active thrust faults are very low (<1 mm yr^{-1}).

Looking at the fault kinematics along the Khazar thrust north of the range suggest that it can be divided into two segments; the western segment that is mainly a thrust fault (∼6 mm yr^{-1}) with a slight left lateral strike slip component (2–3 mm yr^{-1}), and the eastern segment that has a thrust component (2–3 mm yr^{-1}) with a high left-lateral strike-slip rate (∼5 mm yr^{-1}). It seems clear also that the eastern and western segment behave differently since the locking depths obtained are significantly different (∼33 km to the west and 10 km to the east). The shallower locking depth for the eastern segment could indicate the dip of the fault is steeper, but we have no constraint on the dip of this segment. It must be pointed out also that the Alborz range was modelled here as one block. We have chosen to do so because the GPS coverage in eastern Alborz is less dense than the western part of the range. A denser network to the east could reveal low deformation within the Alborz range, but this wouldn't significantly modify our conclusions on the present-day kinematic of the range.

Looking at the velocity field in a Dasht-e-Kavir fixed reference frame is very instructive for deciphering the present-day kinematic of the range (Fig. 13). Indeed, for the western Alborz, it is clear that the motion of the SCB relative to the Kavir induces a collision with an obliquity of about 25°. This obliquity has already been reported by several authors (Jackson *et al.* 2002; Allen *et al.* 2003b; Ritz *et al.* 2006) who suggest that strain partitioning occurs in the Alborz range. Our results agree in part with partitioning in the range since the fault slip rates estimated on the southwest boundary of the Alborz show only left-lateral strike slip (Fig. 9). However, even though all the compression seems to occur on the northern Khazar thrust, a left-lateral component also occurs on this fault. Therefore, as suggested by the modelling of the Zagros range (Vernant & Chery 2006), a full strain partitioning (i.e. one pure thrust fault and one pure strike slip fault) seems almost impossible in continental collisions, and the Alborz is another example to support this conclusion. The most interesting feature of the Dasht-e-Kavir fixed reference frame is the very high obliquity of the convergence direction (∼70°) between the SCB and the Dasht-e-Kavir in the eastern part of the Alborz range. The velocities of the sites GRGN, KORD and SHA1 together with the slip rates estimated by the block model show that the shortening in eastern Alborz is very low. This present-day kinematic of eastern Alborz is not consistent with the topography of the range, and suggests that the kinematic of the SCB has changed recently as suggested by Ritz *et al.* (2006), Nazari *et al.* (2009), Landgraf *et al.* (2009) and Ritz (2009). This is further corroborated by the estimate of shortening across the range based on the balanced cross section of Guest *et al.* (2006). The authors suggest that shortening across the range over the past 12 Myr has been higher for the Central Alborz (50–56 km) than for western Alborz (15–18 km).

Our results show that overall present-day shortening rates across central and western Alborz are similar, suggesting that shortening estimated over 12 Myr is not consistent with the one estimated either from GPS observations or geomorphologic studies (Ritz *et al.* 2006; Ritz 2009). Therefore, even though the rate of shortening between Arabia and Eurasia has not significantly changed over the last 10–20 Myr (McQuarrie *et al.* 2003; Vernant *et al.* 2004c; Reilinger *et al.* 2006), the kinematics of the Alborz range has evolved during this time period.

Gravity measurements nearby the GPS site of ABAL suggest that the uplift rate of the range is about 2 to 3.3 ± 1.5 mm yr^{-1} depending on the admittance used to convert the gravity rate of change into an absolute uplift rate. This result is consistent with the uplift rate of $\sim$2 mm yr^{-1} that can be deduced from the drainage incision in northern Alborz, south of the Khazar thrust fault (Antoine *et al.* 2006). This rate is also consistent with 5 mm yr^{-1} of shortening on a thrust fault dipping at 34° to the south, but suggests that either the river does not incise as fast as the topography grows, or that some kind of isostatic compensation of the range occurs in this region. Given that this study and the study of the Baladeh Earthquake (Tatar *et al.* 2007) suggest that the Khazar thrust fault behaves seismically down to $\sim$30 km depth, and that the Alborz is a narrow range and the seismic part of the fault encompasses most of the range (Fig. 5), further suggesting that the whole range could uplift with a constant rate of about 2–3 mm yr^{-1}. Unfortunately the CGPS data span is not long enough to accurately evaluate the uplift rates, and the hydrological effects of water pumping complicate using the gravity measurements south of the Taleghan, Mosha and Firuzkuh faults. Ritz *et al.* (2006) suggest that these faults have a very low normal faulting component, hence the region south of these faults should uplift at a very slightly higher rate that the northern region. The location of this fault system seems to limit the overriding part of the range that is seismically coupled to the south Caspian oceanic basement from the southern foothills of the range. Based on receiver functions cross section (Paul *et al*. 2010), it seems that the deepest part of the root is located below the southern part of the range. Therefore the uplifting processes, although probably linked, could be different south and north of the Taleghan, Mosha and Firuzkuh fault system.

6 CONCLUSION

We have been able to estimate the motion of the SCB accurately for the first time. Our results suggest an important rotation of the SCB relative to Eurasia, which explains the left lateral motion in the Alborz range. The motion of the SCB relative to the Dasht-e-Kavir allows estimating the upper bound of the deformation accommodated by the Alborz range. The slip rates vary along the range, the thrusting component on the Khazar fault changes from 2 mm yr^{-1} to the east to 6 mm yr^{-1} to the west and the left lateral strike-slip rate from 2 to 1 mm yr^{-1} along the Astaneh, Firuzkuh, Mosha and Taleghan faults, and from 5 to 2 mm yr^{-1} along the Khazar fault from east to west. Hence, some partitioning occurs, but not complete partitioning. Given the motion of SCB and Alborz blocks and the V shaped structure of the Alborz range, the deformation cannot be summarized by only two slip rate values as it has been proposed earlier by Vernant *et al.* (2004a), and one needs to take into account along-range slip rate variations. Our results suggest that the eastern Alborz mainly accommodates strike slip deformation, and that the western Alborz accommodates thrusting. These present-day kinematics agree with the results from geomorphologic studies (Ritz *et al.* 2006; Landgraf *et al.* 2009), but not the long-term deformation (see Guest *et al.* 2006; Hollingsworth *et al.* 2008; Ritz 2009). This supports the idea that the kinematics of the range have changed recently due to the change of SCB motion.

The interseismic deformation suggests a deep locking depth on the central-western segment of the Khazar fault ($\sim$30 km) in agreement with the Baladeh earthquake rupture and aftershocks (Tatar *et al.* 2007). Furthermore, our AG observations suggest that the part of the range seismically coupled on the Khazar thrust fault uplifts with a rate of 1–5 mm yr^{-1}, in agreement with the terrace uplift reported north of the range (Antoine *et al.* 2006).

ACKNOWLEDGMENTS

This work was realized in the frame of a co-operative research agreement between INSU-CNRS (DYETI, RNCC), MAE (French Foreign Office Ministry) and National Cartographic Center (NCC, Tehran). We thank all the teams who went out in the field to collect the data. We are grateful to R. Reilinger and an anonymous reviewer for their constructive comments on this manuscript and their tremendous help to improve our English. We are also thankful to Jean Paul Boy (EOST, Louis Pasteur University, Strasbourg, France) for providing the 2000–2007 hydrological gravity affect from the ECMWF and LadWorld global hydrological models.

REFERENCES

Allen, M., Ghassemi, M.R., Sharabi, M. & Qorashi, M., 2003a. Accomodation of late Cenozoic oblique shortening in the Alborz range, Iran, *J. Struct. Geol.,* **25,** 659–672.

Allen, M.B., Vincent, S.J., Alsop, I., Ismail-zadeh, A. & Flecker, R., 2003b. Late Cenozoic deformation in the South Caspian region: effects of a rigid basement block within a collision zone, *Tectonophysics,* **366,** 223–239.

Allen, M.B. *et al*., 2004. Late Cenozoic reorganization of the Arabia-Eurasia collision and the comparison of short-term and long-term deformation rates, *Tectonics,* **23,** TC2008, doi:10.1029/2003TC001530.

Ambraseys, N.N. & Melville, C.P., 1982. *A History of Persian Earthquakes,* Cambridge University Press, New York.

Andersen, O.B. & Hinderer, J., 2005. Global inter-annual gravity changes from GRACE: early results, *Geophys. Res. Lett.,* **32,** L01402, doi:10.1029/2004GL020948.

Antoine, P., Bahain, J.J., Berillon, G. & Asgari-Khaneghah, A., 2006. Tuf calcaire et séquence alluviale en contexte tectonique actif: la formation de Baliran (province du Mazandaran, Iran), *Quaternaire,* **17,** 321–331.

Ashtari, M., Hatzfeld, D. & Kamalian, N., 2005. Microseismicity in the region of Tehran, *Tectonophysics,* **395,** 193–208.

Axen, G.J., Lam, P.S., Grove, M. & Stockli, D.F., 2001. Exhumation of the west-central Alborz mountains, Iran, Caspian subsidence, and collision-related tectonics, *Geology,* **6,** 559–562.

Bachmanov, D.M., Trifonov, V.G., Hessami, K.T., Kozhurin, A.I., Ivanova, T.P., Rogozhin, E.A., Hademi, M.C. & Jamali, F.H., 2004. Active faults in the Zagros and central Iran, *Tectonophysics,* **380,** 221–241.

Berberian, M., 1981. *Active Faulting and Tectonics of Iran, in Zagros-Hindu Kush-Himalaya Geodynamic Evolution,* pp. 33–69, AGU, Geodyn. Ser.

Berberian, M., 1983. The southern Caspian: a compressional depression floored by a trapped, modified oceanic crust, *Can. J. Earth Sci.,* **20**(2), 163–183.

Berberian, M. & Yeats, R. S., 1999. Patterns of historical earthquake rupture in the Iranian Plateau, *Bull. seism. Soc. Am.,* **89,** 120–139.

Berberian, M. & Yeats, R. S., 2001. Contribution of archaeological data to studies of earthquakes history in the Iranian plateau, *J. Struct. Geol.,* **23,** 563–584.

Dong, D., Herring, T.A. & King, R.W., 1998. Estimating regional deformation from a combination of space and terrestrial geodetic data, *J. Geodyn.,* **72,** 200–211.

Engdahl, E.R., Jackson, J.A., Myers, S.C., Bergman, E.A. & Priestley, K., 2006. Relocation and assessment of seismicity in the Iran region, *Geophys. J. Int.,* **167,** 761–778.

Feigl, K.L. *et al*., 1993. Space geodetic measurement of crustal deformation in central and southern California, *J. Geophys. Res.,* **98,** 21 677–21 712.

Gelb, A., 1974. *Applied Optimal Estimation,* MIT Press, Cambridge, MA.

Goetze, C. & Evans, B., 1979. Stress and temperature in the bending lithosphere as constrained by experimental rock mechanics, *Geophys. J. R. astr. Soc.,* **59,** 463–478.

Guest, B., Axen, G.J., Lam, P.S. & Hassanzadeh, J., 2006. Late Cenozoic shortening in the west-central Alborz Mountains, northern Iran, by combined conjugate strike-slip and thin-skinned deformation, *Geosphere,* **2,** 35–52.

Herring, T.A., King, R.W. & McClusky, S.C., 2009a. *GAMIT reference manual, Release 10.3,* Massachussets Institute of Technology, Cambridge, MA.

Herring, T.A., King, R.W. & McClusky, S.C., 2009b. *GLOBK reference manual, Release 10.3,* Massachussets Institute of Technology, Cambridge, MA.

Herring, T.A., King, R.W. & McClusky, S.C., 2009c. *Introduction to GAMIT/GLOBK, Release 10.35,* Massachussetts Institute of Technology, Cambridge, MA.

Hollingsworth, J., Jackson, J., Walker, R. & Nazari, H., 2008. Extrusion tectonics and subduction in the eastern South Caspian region since 10 Ma, *Geology,* **36,** 763–766, doi:10.1130/G25008A.1.

Jackson, J.A. & McKenzie, D.P., 1984. Active tectonics of the Alpine-Himalayan Belt between western Turkey and Pakistan, *Geophys. J. R. astr. Soc.,* **77,** 185–246.

Jackson, J.A., Priestley, K., Allen, M. & Berberian, M., 2002. Active tectonics of the South Caspian Basin, *Geophys. J. Int.,* **148,** 214–245.

James, T.S. & Ivins, E.R., 1998. Predictions of Antarctic crustal motions driven by present-day ice sheet evolution and by isostatic memory of the Last Glacial Maximum, *J. geophys. Res.,* **103,** 4993–5017.

Karner, G.D. & Watts, A.B., 1983. Gravity-anomalies and flexure of the lithosphere at mountain ranges, *J. geophys. Res.,* **88,** 449–477.

Landgraf, A., Ballato, P., Strecker, M.R., Friedrich, A., Tabatabaei, S.H. & Shahpasandzadeh, M., 2009. Fault-kinematic and geomorphic observations along the North Tehran Thrust and Mosha Fasham Fault, Alborz mountains Iran: implications for fault-system evolution and interaction in a changing tectonic regime, *Geophys. J. Int.,* **177,** 676–690.

Larson, K.M. & van Dam, T., 2000. Measuring postglacial rebound with GPS and absolute gravity, *Geophys. Res. Lett.,* **27,** 3925–3928.

Lyard, F., Lefevre, F., Letellier, T. & Francis, O., 2006. Modelling the global ocean tides: modern insights from FES2004, *Ocean Dyn.,* **56,** 394–415.

Masson, F., Chery, J., Hatzfeld, D., Martinod, J., Vernant, P., Tavakoli, F. & Ghafory-Ashtiani, M., 2005. Seismic versus aseismic deformation in Iran inferred from earthquakes and geodetic data, *Geophys. J. Int.,* **160,** 217–226.

Masson, F., Anvari, M., Djamour, Y., Walpersdorf, A., Tavakoli, F., Daignieres, M., Nankali, H. & Van Gorp, S., 2007. Large-scale velocity field and strain tensor in Iran inferred from GPS measurements: new insight for the present-day deformation pattern within NE Iran, *Geophys. J. Int.,* **170,** 436–440.

McCaffrey, R., 2002. Crustal block rotations and plate coupling. in *Plate Boundary Zones,* pp. 101–122, eds Stein, S. & Freymueller, J. T., AGU Geodynamics Series.

McQuarrie, N., Stock, J.M., Verdel, C. & Wernicke, B.P., 2003. Cenozoic evolution of Neotethys and implications for the causes of plate motions, *Geophys. Res. Lett.,* **30,** doi:10.1029/2003GL017992.

Meade, B.J. & Hager, B.H., 2005. Block models of crustal motion in southern California constrained by GPS measurements, *J. geophys. Res.,* **110**, B04402, doi:10.1029/2004JB003331.

Meade, B.J., Hager, B.H., McClusky, S., Reilinger, R., Ergintav, S., Lenk, O., Barka, A. & Özener, H., 2002. Estimates of seismic potential in the Marmara Sea regions from block models of secular deformation constrained by Global Positioning System Measurements, *Bull. seism. Soc. Am.,* **92,** 208–215.

Meurers, B., Van Camp, M. & Petermans, T., 2007. Correcting superconducting gravity time-series using rainfall modelling at the Vienna and Membach stations and application to Earth tide analysis, *J. Geodyn.,* **81,** 703–712.

Nazari H., Ritz, J.-F., Shafei, A., Ghassemi, A., Salamati, R., Michelot, J.-L. & Massault, M., 2009. Morphological and paleoseismological analyses of the Taleghan fault, Alborz, Iran, *Geophys. J. Int,* **178,** 1028–1041, doi:10.1111/j.1365-246X.2009.04173.x.

Nazari, H., Ritz, J.-F., Salamati, R., Shahidi, A., Habibi, H., Ghorashi & Karimi Bavandpur, A., 2010. Distinguishing between fault scarps and shore lines: the question of the nature of the Rey and Kahrizak features in Tehran region, *Terra Nova*, **22**, 227–237, doi:10.1111/j.1365-3121.2010.00938.x.

Okada, Y., 1985. Surface deformation due to shear and tensile faults in a half-space, *Bull. seism. Soc. Am.,* **75,** 1135–1154.

Okada, Y., 1992. Internal deformation due to shear and tensile faults in a half-space, *Bull. seism. Soc. Am.,* **82,** 1018–1040.

Paul, A., Hatzfeld, D., Kaviani, A., Tatar, M. & Péquegnat, C., 2010. Seismic imaging of the lithospheric structure of the Zagros mountain belt (Iran), *Tectonic and Stratigraphic Evolution of Zagros and Makran during the Meso-Cenozoic,* eds, Leturmy, P. & Robin, C., Geol. Soc. London, Spec. Pub., in press.

Reilinger, R. *et al*., 2006. GPS constraints on continental deformation in the Africa-Arabia-Eurasia continental collision zone and implications for the dynamics of plate interactions, *J. geophys. Res.,* **111,** B05411, doi:10.1029/2005JB004051.

Ritz, J.-F., 2009. Extrusion tectonics and subduction in the eastern South Caspian region since 10 Ma: COMMENT, *Geology,* **37,** e191, doi:10.1130/G25627C.1.

Ritz, J.-F., Nazari, H., Ghassemi, A., Salamati, R., Shafei, A., Solaymani, S. & Vernant, P., 2006. Active transtension inside central Alborz: a new insight into northern Iran-southern Caspian geodynamics, *Geology,* **34,** 477–480.

Savage, J. & Burford, R., 1973. Geodetic determination of relative plate motion in Central California, *J. geophys. Res.,* **95,** 4873–4879.

Solaymani, S., Ritz, J-F. & Abbassi, M., 2010. Analysing the junction between the Mosha and the North Tehran active faults, *Tectonophysics*, in press.

Tatar, M., Jackson, J., Hatzfeld, D. & Bergman, E., 2007. The 2004 May 28 Baladeh earthquake (M-w 6.2) in the Alborz, Iran: overthrusting the South Caspian Basin margin, partitioning of oblique convergence and the seismic hazard of Tehran, *Geophys. J. Int.,* **170,** 249–261.

Tchalenko, J.S., 1975. Seismotectonic framework of north tehran fault, *Tectonophysics,* **29,** 411–420.

Van Camp, M., Williams, S.D.P. & Francis, O., 2005. Uncertainty of absolute gravity measurements, *J. geophys. Res.,* **110,** B05406, doi:10.1029/2004JB003497.

Vernant, P. & Chery, J., 2006. Mechanical modelling of oblique convergence in the Zagros, Iran, *Geophys. J. Int.,* **165,** 991–1002.

Vernant, P. *et al*., 2004a. Deciphering oblique shortening of central Alborz in Iran using geodetic data, *Earth planet. Sci. Lett.,* **223,** 177–185.

Vernant, P. *et al*., 2004b. Deciphering oblique shortening of central Alborz in Iran using geodetic data, *Earth planet. Sci. Lett.,* **223,** 177–185.

Vernant, P. *et al*., 2004c. Present-day crustal deformation and plate kinematics in the Middle East constrained by GPS measurements in Iran and northern Oman, *Geophys. J. Int.,* **157,** 381–398.

Wahr, J., Dazhong, H. & Trupin, A., 1995. Predictions of vertical uplift caused by changing polar ice volumes on a viscoelastic earth, *Geophys. Res. Lett.,* **22,** 977–980.

Wahr, J., Swenson, S., Zlotnicki, V. & Velicogna, I., 2004. Time-variable gravity from GRACE: first results, *Geophys. Res. Lett.,* **31,** L11501, doi:10.1029/2004GL019779.

Walpersdorf, A. *et al*., 2006. Difference in the GPS deformation pattern of north and central zagros (Iran), *Geophys. J. Int.,* **167,** 1077–1088.

Watts, A.B., Bodine, J.H. & Steckler, M.S., 1980. Observations of flexure and the state of stress in the oceanic lithosphere, *J. geophys. Res.,* **85,** 6369–6376.

Wenzel, H.-G., 1994. Earth tide analysis package ETERNA 3.0, *Bulletin d'Informations des Marées Terrestres,* **118,** 8719–8721.